

Structural, electrical, and optical properties of hydrogen-doped ZnO films

Achim Kronenberger,* Angelika Polity, Detlev M. Hofmann, and Bruno K. Meyer
I. Physics Institute, Justus-Liebig-University, Heinrich-Buff-Ring 16, 35392 Giessen, Germany

André Schleife†

*Condensed Matter and Materials Division, Lawrence Livermore National Laboratory, Livermore, California 94550, USA
 and European Theoretical Spectroscopy Facility (ETSF)*

Friedhelm Bechstedt

*Institut für Festkörpertheorie und -optik, Friedrich-Schiller-Universität, Max-Wien-Platz 1, 07743 Jena, Germany
 and European Theoretical Spectroscopy Facility (ETSF)*

(Received 19 July 2012; published 28 September 2012)

Hydrogen doped ZnO thin films were deposited by radio frequency magnetron sputtering from a ceramic target on *c*-plane sapphire and fused silica using H₂ and O₂ as reactive gases. Structural analysis revealed that all films are polycrystalline with the *c* axis oriented perpendicularly to the substrate surface. The lateral grain size was strongly affected by the oxygen content of the sputtering gas and decreased dramatically above a critical content of 4.5 %. We were able to adjust the carrier density of the films by the deposition parameters to any value between 10¹⁴ and 2 × 10²⁰ cm⁻³. Using temperature-dependent Hall-effect measurements we identified thermionic emission over Coulomb-barriers created by surface trap states at the grain boundaries and tunneling effects to dominate the carrier transport. Preparing and thoroughly characterizing the films is a prerequisite for our investigation of the dependence of the optical band gap energy on the carrier density. We use results from experiment as well as first-principles calculations (including Burstein-Moss shift, band gap renormalization, and excitonic effects) in order to understand the mechanisms that determine how free electrons influence the energy position of the optical absorption onset.

DOI: [10.1103/PhysRevB.86.115334](https://doi.org/10.1103/PhysRevB.86.115334)

PACS number(s): 61.72.uj, 73.61.Ga, 74.62.Dh, 78.66.Hf

I. INTRODUCTION

Transparent conductive oxides (TCO) are used as contacts in flat panel displays and solar cells whenever transparency and low electrical resistivity are required. Over the last years not only the demand for these highly conducting materials with carrier densities in the range of 10²⁰ to 10²¹ cm⁻³ increased but the TCOs became building blocks for transparent electronic devices like diodes, thin film transistors, and even integrated circuits.¹ While indium-tin oxide still has the highest performance, it might suffer from a strong increase of production cost; indium has been identified as a *near-critical material* due to the risk that reserves will be exhausted in the near future.^{2,3} Aluminum doped ZnO films offer particularly promising properties and are a potential alternative to replace indium-tin oxide. In addition, E. Mollwo⁴ and D. G. Thomas *et al.*⁵ were the first to discover in the 1950's that the resistivity of ZnO strongly decreases upon the diffusion of hydrogen into bulk crystals. For technological applications but also a better understanding of hydrogen doping, a precise control of the structural properties of the TCOs are as desirable as a deep understanding of their electrical and optical properties.

The formation of a shallow donor level due to hydrogen incorporation was described theoretically by Van de Walle⁶ and experimentally proven by several groups.^{7,8} At present there are two types of shallow hydrogen donors proposed by first-principles calculations. One is formed when a hydrogen atom is incorporated on an interstitial bond-centered lattice site⁶ (H_{BC}), while the other is caused by the occupation of an

oxygen vacancy by a hydrogen atom (H_O).⁹ Lavrov *et al.*¹⁰ investigated these two hydrogen donors in bulk ZnO and found activation energies of 53 meV for H_{BC} and 47 meV for H_O, respectively. They also found that H_{BC} is unstable by annealing above 190°C and provided evidence that H_{BC} defects recombine to electrically inactive H₂ molecules. The thermal stability of H_O was mainly studied by photoluminescence spectroscopy. It gives rise to the I₄ donor bound exciton at 3362.8 meV. In these investigations it was shown that H_O is unstable against annealing at temperatures above 500 °C.^{11,12} In addition to the configurations mentioned above, there are indications for further hydrogen-related shallow donors: after hydrogenation two donors with ionization energies of 35 and 42 meV appear,^{8,10} however, so far, the microscopic structure of these defects is unknown.

Besides the investigation of hydrogen in bulk ZnO also hydrogen doping of thin films by reactive radio frequency sputtering was reported.^{13,14} Adding hydrogen to the deposition process or post annealing in hydrogen atmosphere is also used to improve the conductivity of films already doped with aluminum or gallium donors.^{15–21}

While the carrier density of ZnO TCO layers can be influenced by the oxygen content of the sputtering gas, a fine tuning of the electrical properties is hard to achieve since the dependence on the oxygen content is rather sensitive²² when depositing at room temperature. This is the case for nominally undoped ZnO films as well as for films doped with group-III elements.^{22,23} Therefore it can be hard to adjust the carrier density to the value needed for a specific application. Moreover, the free electrons that are introduced into the

samples are known to influence the energy position of the optical absorption edge. However, the underlying mechanisms are not conclusively understood (see, e.g., Refs. 24–26 and references therein).

In this work, we found that using a mixture of hydrogen and oxygen as reactive gas in a sputter deposition process is suitable for a good control of the electric properties of ZnO thin films deposited at room temperature. We were able to adjust the carrier density in a wide range from 10^{14} up to $2 \times 10^{20} \text{ cm}^{-3}$. Besides the tuning of the electrical properties, we analyzed the dependence of the crystal structure and the growth mechanism on the deposition parameters and the optical film quality. In Sec. II, details on the techniques used for preparing and characterizing the samples are given. We present results for the structural, electrical, and optical properties of our samples in Sec. III. In addition, by using modern *parameter-free* calculations we go beyond previous theoretical schemes²⁷ (that merely relied on two-band effective mass approximations and also neglect excitonic effects) to describe the relationship between the free-electron concentration and the shift of the optical-absorption edge. Finally, Sec. IV concludes the paper.

II. EXPERIMENTAL DETAILS

Hydrogen doped ZnO films were deposited by radio frequency (RF) magnetron sputtering from a 3 in. high purity (99.999 %) ceramic ZnO target. A constant hydrogen to argon ratio of 1/12 was used which equals the optimum ratio observed in previous experiments to obtain a low film resistivity.¹³ Additionally oxygen was added to the argon hydrogen mixture varying the content from 0% to 17% [$\text{O}_2/(\text{Ar} + \text{H}_2 + \text{O}_2)$]. The purities of the argon, molecular hydrogen (H_2), and molecular oxygen (O_2) gas were 99.999%, 99.999%, and 99.998%, respectively. The RF power was fixed at 200 W and the base chamber pressure was below 1×10^{-4} Pa. The work pressure was set between 0.4 and 0.9 Pa depending on the total gas flow. Films were grown on fused silica and *c*-sapphire [(0001)-oriented] substrates.

The crystal structure of the films was analyzed with a Siemens D5000 X-ray diffractometer in Bragg-Brentano geometry using the K_α radiation of the copper anode. Scanning electron microscopy (SEM) images of the surface and cross-section of the films were taken with a Leo Gemini 982 microscope. Hall-effect measurements were performed in the Van der Pauw arrangement with an applied magnetic field of 1 T. For these measurements the samples were placed in an evacuated cryostat allowing temperatures between 35 and 400 K. To obtain ohmic contacts indium was soldered onto the layers at 200 °C. A Lambda 900 spectrometer from Perkin-Elmer Instruments was used to measure the optical transmittance in a wavelength range from 250 to 3000 nm. The film thickness was determined from the interference fringes in the transmittance spectra.

To eliminate thickness-dependent effects when comparing the results for different deposition parameters all films were grown 500 ± 50 nm thick. Additionally, a series with film thicknesses from 10 up to 3000 nm were deposited for further analysis.

III. RESULTS AND DISCUSSION

A. Structural properties

X-ray diffraction analyses revealed that all films are polycrystalline with the *c* axis oriented perpendicularly to the substrate surface. Therefore the (0002) reflection is the only visible one in the $\theta/2\theta$ scan besides the substrate related reflections observed when growing on sapphire. Figure 1(a) shows, for example, the diffraction pattern (normalized intensities) of a hydrogen doped film deposited without oxygen (dashed line) and a film deposited with the highest oxygen flow used in our experiments (solid line), both grown on sapphire. From the angular position of the (0002) reflection, the *c*-axis lattice constant can be derived. For hydrogen doped films deposited without oxygen, we observed an increase in lattice constant ($c_{\text{dop}} \approx 5.26 \text{ \AA}$) compared to nominally undoped ZnO films ($c_{\text{und}} \approx 5.23 \text{ \AA}$). The latter was prepared with similar deposition parameters and film thickness, as the hydrogen-doped film. Its diffraction position is marked by the dotted line. This value for the lattice constant is already larger than the literature value of bulk ZnO ($c_{\text{bulk}} \approx 5.21 \text{ \AA}$, dot-dashed line).²⁸ Adding oxygen to the sputtering process induces a *c*-axis shrinkage for the films grown on sapphire approaching the value of the undoped films. A similar behavior was not observed for the films on fused silica where the *c*-axis lattice parameter stayed more or less constant.

Variations of the *c*-axis lattice constant due to stress are commonly observed for films deposited by sputtering techniques and reduce with increasing film thickness since the material relaxes.²⁹ A possible explanation for the additional increase of the lattice constant with hydrogen doping is either higher stress due to the deposition process, or the incorporation of impurities that expand the lattice. According to the hydrogen doping process, favored candidates in this case are the incorporation of hydrogen on an interstitial position (for instance H_{BC}) or an oxygen reduction of the material that might lead to a higher concentration of interstitial zinc atoms (Zn_i). A larger

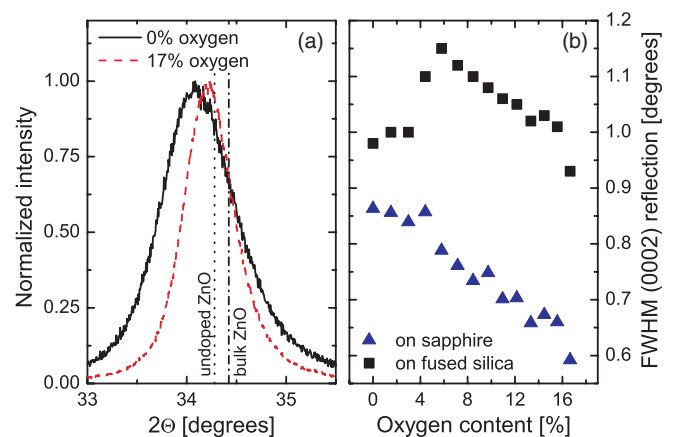


FIG. 1. (Color online) (a) X-ray diffraction pattern of a hydrogen doped film deposited on sapphire without oxygen (black solid line) and a hydrogen doped film deposited with 17% oxygen (red dashed line) in the sputtering gas. Dotted lines mark the (0002) peak position of bulk ZnO and nominally undoped sputter deposited ZnO films. (b) Dependence of the full width at half maximum (FWHM) of the (0002) reflection on the oxygen content of the sputtering gas.

c-axis lattice constant upon hydrogen doping was reported before and is in most cases attributed to the incorporation of H_{BC} .¹⁴ Park *et al.*³⁰ found an increased unit cell volume which is in accordance with calculations by Van de Walle on H_{BC} .⁶ Since we observe only the (0002) reflection in the diffraction patterns no information on the unit cell volume is provided and a distinction between whether the lattice expansion is caused by stress or impurity incorporation is not possible. Previous experiments, however, propose that H_{BC} is not the dominant defect in our films since we observed the hydrogen content and electrical properties to be stable for annealing of 200 °C where H_{BC} induced donors should vanish already.¹³

Figure 1(b) shows the full width at half maximum (FWHM) of the (0002) reflection and its dependence on the oxygen content of the sputtering gas. With hydrogen doping the FWHM increases compared to the undoped reference samples, where we typically observe values around 0.2° to 0.3°, to approximately 0.85° for films on sapphire and 0.98° for films on fused silica. Adding oxygen to the sputtering process decreases the FWHM continuously for the films deposited on sapphire, while for the films on fused silica the FWHM suddenly increases to 1.15° at an oxygen content of the sputtering gas of about 4.5%. From there on, a steady decrease with increasing oxygen content is observed.

A smaller FWHM indicates a better crystalline quality and is assigned to a bigger grain size. Since the (0002) reflection is correlated only to planes perpendicular to the *c* axis the information on the grain size is also limited to this direction. To provide direct information on the lateral grain size we took surface images via SEM. Figure 2 shows surface and cross-sectional images of hydrogen doped films deposited with and without oxygen flow. By depositing without oxygen a lateral grain size around 100 to 200 nm is reached at a film thickness of 500 nm [cf. Fig. 2(a)]. In the following, these type of films are referred to as “big crystallites.” When increasing the oxygen flow the grain size stays constant until for oxygen contents of the sputtering gas higher than 4.5%

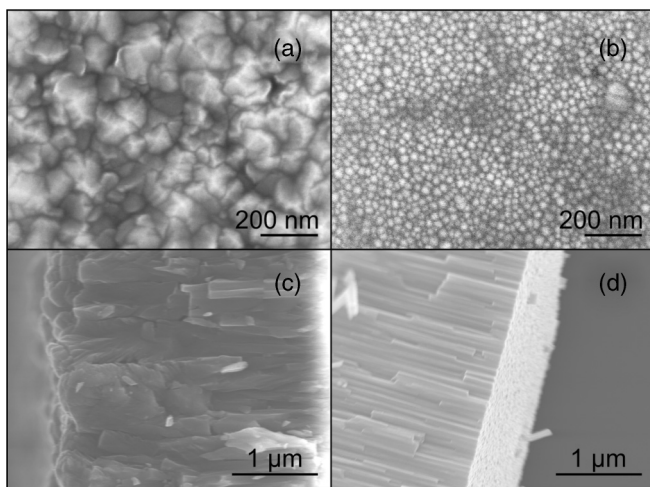


FIG. 2. SEM images of hydrogen doped films deposited without (a) and (c) and intermediate oxygen flow (b) and (d). The surface images (a) and (b) were taken from two 500-nm-thick films, while for the cross-section view (c) and (d) films with 3000-nm thickness are displayed.

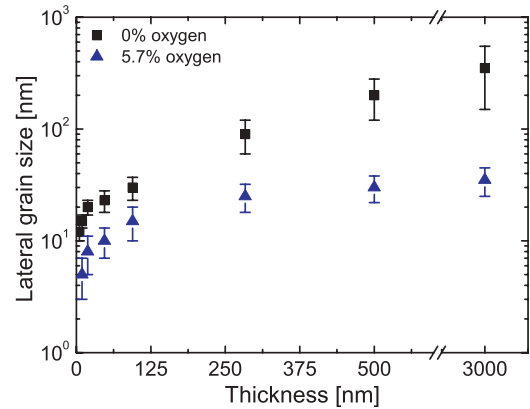


FIG. 3. (Color online) Dependency of the lateral grain size derived from SEM surface images on the film thickness for two different oxygen contents of the sputtering gas.

the growth behavior changes resulting in lateral grain sizes of about 30 nm with a much lower size distribution [Fig. 2(b), referred to as “small crystallites”]. This change coincides with the sudden increase of the FWHM of the (0002) reflection already described before. The different growth behavior is also visible in the cross-section images. The films deposited without oxygen start to form small crystallites on the substrate which combine to bigger ones with increasing film thickness [cf. Fig. 2(c)]. On the contrary, the films deposited with high oxygen content show a homogeneous columnar structure where the lateral grain size is almost constant over the whole film thickness [see Fig. 2(d)].

We further investigated the dependence of the grain size on the film thickness by analyzing the SEM surface images to prove the assumptions from the cross-section images (see Fig. 3, note the logarithmic scale). For the films composed of “big crystallites,” the lateral grain size is strongly thickness dependent and increases continuously for thicker films. Additionally, the grains are widely distributed in size. In the oxygen flow region where the homogeneous columnar growth with the “small crystallites” occurs the lateral grain size stays almost constant for film thicknesses above approximately 200 nm.

The SEM images, in accordance with the decrease of the FWHM of the (0002) reflection, show an increasing grain size perpendicular to the substrate with increasing oxygen flow [compare Figs. 2(c) and 2(d)]. Nevertheless, the size evaluated from the diffraction patterns by the Scherrer equation³¹ is much smaller than the one suggested from the SEM images that show crystallite lengths in the region of the film thickness for high oxygen flows. Such discrepancies have been reported and were assigned to a broadening of the FWHM due to instrumental and stress-induced effects.³² Additionally, the crystal quality (e.g., stacking faults) is an influencing factor.³³ For aluminum doped ZnO films, transmission electron microscopy (TEM) investigations also revealed that columnar grains do not have to be single crystals but can consist of smaller slightly tilted crystallites.^{34,35}

B. Electrical properties

The resistivity and carrier density of the hydrogen doped films determined via Hall-effect measurements are shown in

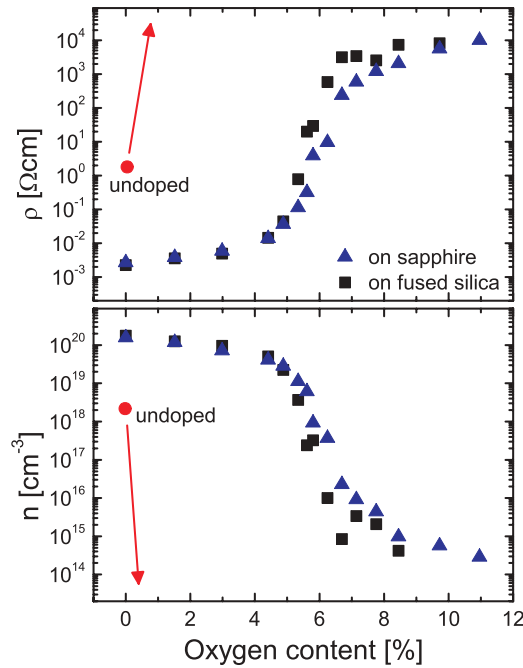


FIG. 4. (Color online) Resistivity (ρ) and carrier density (n) of films deposited with different oxygen content in the sputtering gas. The dots mark the values of nominally undoped ZnO films deposited with the same parameters and the arrows indicate the trends when adding oxygen only.

Fig. 4. With hydrogen doping the resistivity can be decreased over three orders of magnitude to the low $10^{-3} \Omega \text{ cm}$ compared to undoped films grown with similar deposition parameters and film thickness (cf. Fig. 4, red dots). This goes along with an increase of the carrier density from the low 10^{18} cm^{-3} to approximately $2 \times 10^{20} \text{ cm}^{-3}$. Based on our previous studies we used a hydrogen to argon ration of 1/12, which gave the best electrical properties.¹³

The n -type conductivity of nominally undoped sputter deposited ZnO is often attributed to a zinc rich stoichiometry which gives rise to native defects like Zn_i and V_O . However, the oxygen vacancy was calculated to form a 1 eV deep donor (see Ref. 36 and references therein) and should therefore not contribute to the conductivity. Zinc interstitials are known to form shallow donors but there are studies proposing that they will not be stable at room temperature.³⁷ Disregarding the native defects it is likely that impurities originating from the sputter environment, the residual gas, or contamination of the target might be the explanation.

Adding oxygen to the sputtering process of undoped as well as of hydrogen doped ZnO increases the resistivity with increasing oxygen content. While the undoped films get almost instantly insulating for small oxygen contents (arrows in Fig. 4), the hydrogen-oxygen reactive gas mixture enables the possibility to adjust the carrier density to any value between 10^{14} and $2 \times 10^{20} \text{ cm}^{-3}$. The carrier density declines significantly for oxygen contents above 0.045, which coincides with the change in growth behavior detected in the structural investigations. For carrier densities below 10^{16} cm^{-3} , the dependence on the oxygen fraction gets less pronounced until the film resistivity becomes too high to perform further

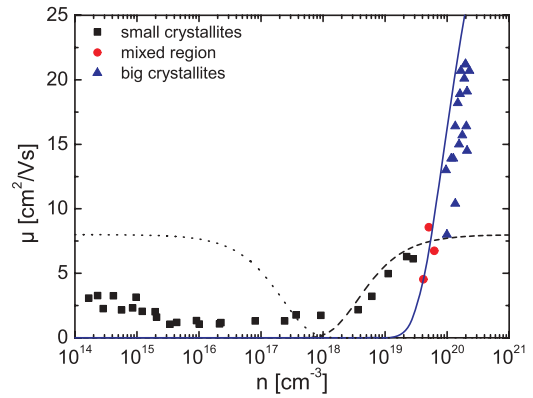


FIG. 5. (Color online) Mobility of the free carriers (μ) plotted against the carrier density (n). Solid, dashed and dotted lines represent fitting results using grain boundary limited transport theory.

measurements. The electrical properties were independent of the substrate used and in additional measurements we also found that the carrier density is not affected by the film thickness (not shown).

The dependence of the Hall mobility on the carrier density is shown in Fig. 5 for the hydrogen doped films. For densities above 10^{18} cm^{-3} , it steadily increases reaching values up to $23 \text{ cm}^2/\text{Vs}$. Such a behavior can be attributed to grain boundary limited transport and was observed in aluminum doped polycrystalline ZnO thin films.^{38,39} For even higher carrier densities scattering at ionized impurities may become dominant in ZnO, which would decrease the mobility again,⁴⁰ but this range is not reached in our samples.

The first comprehensive description of barrier limited transport was given by Seto⁴¹ to explain the results for polycrystalline silicon. He assumed a δ -shaped density of trap states in the band gap forming a Coulomb barrier with an energetic height of Φ_B by capturing electrons from the bulk (in n -type material). This simple model was further improved by Baccarani *et al.*⁴² considering a continuous distribution of trap states. In both models, the transport is dominated by thermionic emission across the grain barriers leading to an effective mobility given by

$$\mu_{\text{eff}} = \mu_0 \exp\left(-\frac{\Phi_B}{k_B T}\right), \quad (1)$$

where T and k_B are the temperature and Boltzmann's constant, respectively. The prefactor μ_0 is regarded as the in-grain mobility and is given by

$$\mu_0 = \frac{eL}{\sqrt{2\pi m^* k_B T}}, \quad (2)$$

where L is the grain size. Equation (2) leads to rather high values which have not been observed for polycrystalline ZnO (e.g., $\mu_0 \approx 2000 \text{ cm}^2/\text{Vs}$ for 100 nm grains at RT). Therefore μ_0 is commonly treated as a fitting parameter.^{39,40}

To calculate the barrier height, Seto derived two expressions assuming on one hand the case of a completely depleted grain where all carriers are captured in the traps and on the other hand the situation where the traps are completely filled and the excess electrons remain in the volume of the grain. The former describes the situation for $nL < Q_T$ and the later for

$nL > Q_T$, where n is the carrier density and Q_T the surface trap density. The barrier height is then given by⁴¹

$$\Phi_B = \frac{e^2 L^2 n}{8\epsilon\epsilon_0}, \quad \text{for } nL < Q_T, \quad (3)$$

and

$$\Phi_B = \frac{e^2 Q_T^2}{8\epsilon\epsilon_0 n}, \quad \text{for } nL > Q_T, \quad (4)$$

where e is the elementary charge, and $\epsilon\epsilon_0$ is the static dielectric constant.

According to the theory our mobility data were fitted for the case $nL > Q_T$ by adjusting Q_T and μ_0 which influence the onset and slope of the mobility limit, respectively. Best results were achieved by treating the films with different grain sizes separately leading to $Q_T \approx 9 \times 10^{12} \text{ cm}^{-2}$ and $\mu_0 \approx 40 \text{ cm}^2/\text{Vs}$ for the “big grains” (solid line in Fig. 5) and $Q_T \approx 2 \times 10^{12} \text{ cm}^{-2}$ and $\mu_0 \approx 8 \text{ cm}^2/\text{Vs}$ for the “small grains” (dashed line in Fig. 5). These trap densities are in the range commonly observed for polycrystalline ZnO thin films which are between 1×10^{12} and $3 \times 10^{13} \text{ cm}^{-2}$ (see Ref. 43 and references therein).

For the in-grain mobility we have to consider that it might not be constant for all films with similar grain sizes. This may especially be the case for the “big crystallites” with a high carrier density and can explain the wide scattering of the mobility values in this range. Therefore the values for μ_0 and Q_T that we obtained should be regarded as upper limits. Nevertheless, it seems reasonable that the in-grain mobility is lower in the smaller crystallites as it is proposed by Eq. (2).

Despite the rather good description for $nL > Q_T$ the data for low carrier densities ($nL < Q_T$) cannot be fitted satisfyingly (dotted line). Neither the predicted mobility drop at $nL = Q_T$ ($n \approx 1 \times 10^{18} \text{ cm}^{-3}$) shows up nor the increase to $\mu_0 \approx 8 \text{ cm}^2/\text{Vs}$ for the lowest carrier densities is observed in the experiments. Instead the mobility is rather constant at about $1\text{--}2 \text{ cm}^2/\text{Vs}$.

To gain further information on the conduction mechanisms, we performed temperature-dependent Hall-effect measurements. In Fig. 6 the carrier density (upper graph) and the mobility (lower graph) of several films are plotted against the inverse temperature. The carrier density becomes temperature independent for densities above $5 \times 10^{18} \text{ cm}^{-3}$, which is typical for a degenerated semiconductor where the Fermi level ϵ_F enters the conduction band. This transition to a metallic-like behavior is given by Mott’s critical density⁴⁴ and for ZnO it is commonly found to be in the mid 10^{18} cm^{-3} range. For densities below, a semiconducting behavior is observed leading to a freeze-out of the free carriers at low temperatures (reverse triangles, Fig. 6, upper graph). By fitting the slope of the data points in the Arrhenius plot, we obtained an activation energy of 43 meV, which is on the order of the values reported for the hydrogen donors in ZnO and matches almost perfectly to the 42 meV donor observed by Lavrov *et al.*¹⁰ However, one should keep in mind that the activation energy derived from Hall-effect measurements cannot necessarily be traced back to a single donor species.

Assuming thermionic emission over grain boundary barriers as the dominant transport mechanism the mobility should be energetically activated. The Arrhenius plot visualizes

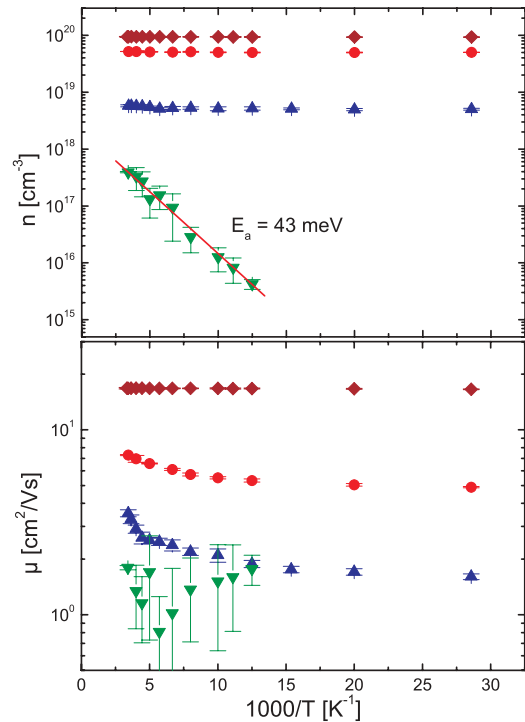


FIG. 6. (Color online) Carrier density (n) (upper graph) and Hall-mobility (μ) (lower graph) plotted against the reciprocal temperature for films with different room-temperature carrier density.

such a behavior around room temperature (Fig. 6, lower graph). The thermal activation is getting less significant with increasing carrier density, and therefore higher mobility. This is in accordance with Seto’s model since the barrier height should decrease in this range. But the results reveal also that thermionic emission alone cannot describe the complete temperature dependence sufficiently since the decrease of the mobility is getting less pronounced for low temperatures. In addition, the activation of the mobility vanishes for the highest carrier density around $1 \times 10^{20} \text{ cm}^{-3}$.

This behavior can be explained by assuming additional tunneling of carriers through the barrier. It leads to a temperature independent fraction of the total mobility. The mobility rises above this constant value at high temperatures where thermionic emission becomes dominant. Tunneling of carriers is strongly affected by the barrier’s width and therefore the effect is more pronounced for samples with high carrier densities and smaller barrier widths. Tunneling effects were reported also for polycrystalline aluminum doped ZnO by several groups and also found to be dominant especially for high carrier densities,^{33,34,45} which is in agreement with our results.

For films with carrier densities below Mott’s critical density,⁴⁴ the temperature dependence of the mobility could not be analyzed satisfactorily since the freeze-out of the carrier leads to a high resistive behavior and therefore to large measurement errors at low temperatures (cf. Fig. 6, lower graph, reversed triangles).

C. Optical properties

Figure 7 shows examples of the transmittance spectra of a highly conductive hydrogen doped film ($n = 2 \times 10^{20} \text{ cm}^{-3}$,

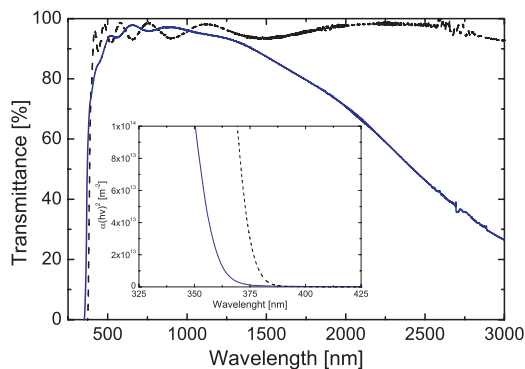


FIG. 7. (Color online) Spectral transmittance of highly conductive (solid line, $n = 2 \times 10^{20} \text{ cm}^{-3}$) and an insulating (dashed line) film. The inset shows the square of the absorption coefficient in the band edge region.

blue solid line) and an insulating film deposited with additional high oxygen flow (black dashed line). The reduced transmittance of highly doped films in the near infrared region is attributed to absorption and reflection by free carriers. The onset of the decay in transmittance depends on the plasma frequency which increases with increasing carrier density and therefore shifts to lower wavelengths. For high carrier density, also a blue shift of the fundamental absorption is observed (inset Fig. 7).

In order to explain the energy position of the optical-absorption onset in a doped system several effects have to be taken into account:²⁵ (i) In the case of high doping, the Fermi level enters the conduction band and, consequently, electrons can no longer be excited from the valence band maximum to the minimum of the conduction band. Instead higher energies are needed to reach unoccupied states. This so-called Pauli blocking leads to an *increase* of the optical band gap which is referred to as Burstein-Moss shift (BMS).^{46,47} (ii) In addition, the free electrons in an n -doped material screen the electron-electron interaction which leads to a band gap narrowing that counteracts the widening due to the BMS. This effect is called band gap renormalization (BGR) and also has to be taken into account. (iii) The screening of the electron-electron interaction due to the free electrons also influences²⁵ the binding energy and the oscillator strength of bound excitonic states that are characteristic for undoped ZnO.^{48–50} Both the binding energy and the oscillator strength are strongly reduced in the presence of free electrons.²⁵ (iv) In materials very similar to ZnO, such as SnO₂⁵¹ or nitride semiconductors,⁵² free-carrier absorption plays a role and can, in the case of high doping, even form the onset of the optical absorption.⁵¹ However, due to the energy distance of the lowest conduction band and the second-lowest one in ZnO, this effect is negligible for the free-electron concentrations studied in this work.^{53,54}

Considering the effects (i)–(iii), the optically detected band-gap energy, more precisely, the position of the absorption onset, in a system with free electrons is given by

$$E_g(n) = E_g^{\text{ZnO}} + \Delta E_{\text{BMS}}(n) + \Delta E_{\text{BGR}}(n) - E_B^{\text{exc}}(n). \quad (5)$$

In this equation, E_g^{ZnO} is the gap of undoped ZnO (3.35 eV was used in this work), $\Delta E_{\text{BMS}}(n)$ and $\Delta E_{\text{BGR}}(n)$ describe the

BMS and the BGR, respectively, and the binding energy of the lowest bound exciton $E_B^{\text{exc}}(n)$ is subtracted. In order to compute $\Delta E_{\text{BMS}}(n)$ and $\Delta E_{\text{BGR}}(n)$, we employ the electronic structure of ZnO computed within the LDA + U + Δ *first-principles* approach (see Refs. 53 and 54 for details). Therefore we go beyond previous effective-mass approximations (see, e.g., Ref. 27 and references therein) and are also able to take excitonic effects into account. In addition, our scheme allows to achieve the very fine sampling of the \mathbf{k} space that is necessary to resolve free-electron densities of about 10^{17} cm^{-3} .

Using the band- and \mathbf{k} -dependent eigenvalues $\varepsilon_n(\mathbf{k})$ we determine the \mathbf{k} -space volume that corresponds to occupied conduction-band states as a function of the position of the Fermi level within the conduction band. The energy difference of the lowest unoccupied conduction-band state and the corresponding valence-band state together with the occupied \mathbf{k} -space volume (that can straightforwardly be related to a doping concentration n) leads to the BMS as depicted in Fig. 8(a). We showed previously²⁶ that this procedure is superior to merely computing the BMS from a parabolic two-band model due to the strong direction dependence and nonparabolicity of the lowest conduction band.

In order to compute the BGR within a *first-principles* framework, it is necessary to take into account the influence of the free-carrier-induced screening. In order to avoid the very high computational cost of performing, for instance, GW calculations for many different doping concentrations along with the very fine \mathbf{k} -point sampling, we rely on the description by Berggren and Sernelius.⁵⁵ They model the BGR as

$$\Delta E_{\text{BGR}}(n) = -\frac{e^2 k_F}{2\pi^2 \varepsilon \varepsilon_0} - \frac{e^2 q_{\text{TF}}}{8\pi \varepsilon \varepsilon_0} \left[1 - \frac{4}{\pi} \arctan\left(\frac{k_F}{q_{\text{TF}}}\right) \right]. \quad (6)$$

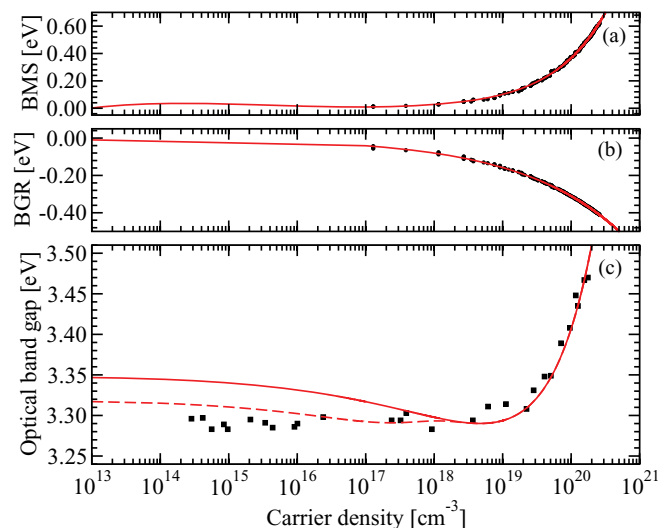


FIG. 8. (Color online) The dependence of the Burstein-Moss shift (a) and the band-gap renormalization (b) as derived from *first-principles* calculations are given as a function of the free-electron density (black dots). The data are interpolated [solid lines in (a) and (b)] and compared to the experimental results (c). The dashed curve in (c) also accounts for the influence of excitonic effects.

The Fermi wave vector k_F and the Thomas-Fermi wave vector q_{TF} are computed according to

$$k_F = \sqrt[3]{3\pi^2 n}, \quad (7)$$

$$q_{TF} = \sqrt{\frac{e^2}{\epsilon_0 \epsilon_{\text{eff}}} \frac{\partial n}{\partial \epsilon_F}}. \quad (8)$$

The term $\partial n / \partial \epsilon_F$ is again derived from the calculated band structure as a function of the free-electron concentration and in Fig. 8(b) the result for $\Delta E_{BGR}(n)$ is depicted.

Figure 8(c) shows the dependence of the detected optical band gap energy on the carrier density along with the theoretical curve taking the BMS and the BGR into account (solid line). This figure shows that the agreement of experiment and theory is particularly good for free-electron concentrations larger than 10^{18} cm^{-3} . The discrepancy for smaller doping levels can be explained by excitonic effects that have not been taken into account so far and also have been neglected in earlier works.^{24,27} The binding energy of the lowest bound excitonic state is about 60 meV in undoped ZnO⁵⁶ and decreases rapidly with an increasing free-electron concentration.²⁵ Here, we use the data for the dependence of the binding energy on the free-electron concentration derived from the solution of the Bethe-Salpeter equation (taking the occupation of the lowest conduction-band states and the screening due to the free electrons into account) in Ref. 25 to approximate $E_B^{\text{exc}}(n)$ [cf. Eq. (5)]. The dashed line in Fig. 8(c) agrees impressively well with the experimental data points over the entire range of n and, hence, can explain the influence of free electrons in the conduction band on the optical band gap. Therefore we find that it is sufficient to account for the BGR that arises due to the free electrons in the sample only. Hence, for hydrogen-doped ZnO, the chemical effects due to the impurity seem to be

negligible, which is in contrast to earlier reports for doped In_2O_3 .²⁴

IV. CONCLUSIONS

We have shown that using a hydrogen-oxygen reactive gas mixture is suitable to adjust the carrier density of ZnO thin films deposited by radio frequency magnetron sputtering to any value between 10^{14} and $2 \times 10^{20} \text{ cm}^{-3}$. The analysis of the structural properties revealed that the lateral grain size of the polycrystalline films decreases dramatically for oxygen contents of the sputtering gas above a critical value of 4.5 %. The room-temperature and temperature-dependent Hall-effect measurements showed that the carrier transport is dominated by thermionic emission over Coulomb-barriers created by surface trap states at the grain boundaries. Additional tunneling effects have to be considered to fully describe the temperature dependence of the Hall mobility. *First-principles* calculations including Burstein-Moss shift, band gap renormalization, and excitonic effects were employed to describe the dependence of the optical band gap energy on the carrier density and are in excellent agreement with the experimental data.

ACKNOWLEDGMENTS

The authors thank S. H. Wei, S. Hamel, D. Steiauf, A. Janotti, and C. G. Van de Walle for fruitful scientific discussions. Financial support by the Deutsche Forschungsgemeinschaft (Project No. Be 1346/20-1) is gratefully acknowledged. Part of this work was performed under the auspices of the U.S. Department of Energy at Lawrence Livermore National Laboratory under Contract DE-AC52-07A27344.

*achim.kronenberger@exp1.physik.uni-giessen.de

†a.schleife@llnl.gov

¹M. Grundmann, H. Frenzel, A. Lajn, M. Lorenz, F. Schein, and H. von Wenckstern, *Phys. Status Solidi A* **207**, 1437 (2010).

²US Department of Energy, Critical Materials Strategy (2011).

³B. K. Meyer and P. J. Klar, *Phys. Status Solidi R* **5**, 318 (2011).

⁴E. Mollwo, *Z. Phys.* **138**, 478 (1954).

⁵D. G. Thomas and J. J. Lander, *J. Chem. Phys.* **25**, 1136 (1956).

⁶C. G. Van de Walle, *Phys. Rev. Lett.* **85**, 1012 (2000).

⁷S. F. J. Cox, E. A. Davis, S. P. Cottrell, P. J. C. King, J. S. Lord, J. M. Gil, H. V. Alberto, R. C. Vilão, J. Piroto Duarte, N. Ayres de Campos, A. Weidinger, R. L. Lichti, and S. J. C. Irvine, *Phys. Rev. Lett.* **86**, 2601 (2001).

⁸D. M. Hofmann, A. Hofstaetter, F. Leiter, H. Zhou, F. Henecker, B. K. Meyer, S. B. Orlinskii, J. Schmidt, and P. G. Baranov, *Phys. Rev. Lett.* **88**, 045504 (2002).

⁹A. Janotti and C. G. Van de Walle, *Nat. Mater.* **6**, 44 (2007).

¹⁰E. V. Lavrov, F. Herklotz, and J. Weber, *Phys. Rev. B* **79**, 165210 (2009).

¹¹G. A. Shi, M. Stavola, S. J. Pearton, M. Thieme, E. V. Lavrov, and J. Weber, *Phys. Rev. B* **72**, 195211 (2005).

¹²B. K. Meyer, H. Alves, D. M. Hofmann, W. Kriegseis, D. Forster, F. Bertram, J. Christen, A. Hoffmann, M. Straßburg, M. Dworzak, U. Haboeck, and A. V. Rodina, *Phys. Status Solidi B* **241**, 231 (2004).

¹³S. Eisermann, A. Kronenberger, M. Dietrich, S. Petznick, A. Laufer, A. Polity, and B. K. Meyer, *Thin Solid Films* **518**, 1099 (2009).

¹⁴L.-Y. Chen, W.-H. Chen, J.-J. Wang, F. C.-N. Hong, and Y.-K. Su, *Appl. Phys. Lett.* **85**, 5628 (2004).

¹⁵T. Minami, T. Miyata, and Y. Ohtani, *Phys. Status Solidi A* **204**, 3145 (2007).

¹⁶H. Chang, F. Wang, J. Wu, C. Kung, and H. Liu, *Thin Solid Films* **518**, 7445 (2010).

¹⁷S. Tark, Y.-W. Ok, M. Kang, H. Lim, W. Kim, and D. Kim, *J. Electroceram.* **23**, 548 (2009).

¹⁸H. Chen, H.-J. Jin, C.-B. Park, and G. C. Hoang, *Trans. Electr. Electron. Mater.* **10**, 93 (2009).

¹⁹J. N. Duenow, T. A. Gessert, D. M. Wood, D. L. Young, and T. J. Coutts, *J. Non-Cryst. Solids* **354**, 2787 (2008).

²⁰B.-Y. Oh, M.-C. Jeong, D.-S. Kim, W. Lee, and J.-M. Myoung, *J. Cryst. Growth* **281**, 475 (2005).

²¹D.-H. Kim, S.-H. Lee, G.-H. Lee, H.-B. Kim, K. H. Kim, Y.-G. Lee, and T.-H. Yu, *J. Appl. Phys.* **108**, 023520 (2010).

- ²²P. F. Carcia, R. S. McLean, M. H. Reilly, and J. G. Nunes, *Appl. Phys. Lett.* **82**, 1117 (2003).
- ²³T. Tsuji and M. Hirohashi, *Appl. Surf. Sci.* **157**, 47 (2000).
- ²⁴A. Walsh, J. L. F. Da Silva, and S.-H. Wei, *Phys. Rev. B* **78**, 075211 (2008).
- ²⁵A. Schleife, C. Rödl, F. Fuchs, K. Hannewald, and F. Bechstedt, *Phys. Rev. Lett.* **107**, 236405 (2011).
- ²⁶A. Schleife and F. Bechstedt, *Proc. SPIE* **8263**, 826309 (2012).
- ²⁷J. Jia, A. Takasaki, N. Oka, and Y. Shigesato, *J. Appl. Phys.* **112**, 013718 (2012).
- ²⁸H. Morkoç and U. Özgür, *Zinc Oxide - Fundamentals, Materials and Device Technology* (Wiley-VCH Verlag GmbH & Co. KGaA, Weinheim, 2009).
- ²⁹B.-Z. Dong, G.-J. Fang, J.-F. Wang, W.-J. Guan, and X.-Z. Zhao, *J. Appl. Phys.* **101**, 033713 (2007).
- ³⁰Y. R. Park, J. Kim, and Y. S. Kim, *Appl. Surf. Sci.* **255**, 9010 (2009).
- ³¹P. Scherrer, *Nachrichten von der Gesellschaft der Wissenschaften zu Göttingen* **2**, 98 (1918).
- ³²N. H. Kim and H. W. Kim, *Mater. Lett.* **58**, 938 (2004).
- ³³A. Asadov, W. Gao, Z. Li, J. Lee, and M. Hodgson, *Thin Solid Films* **476**, 201 (2005).
- ³⁴S. Brehme, F. Fenske, W. Fuhs, E. Nebauer, M. Poschenrieder, B. Selle, and I. Sieber, *Thin Solid Films* **342**, 167 (1999).
- ³⁵I. Sieber, N. Wanderka, I. Urban, I. Dörfel, E. Schierhorn, F. Fenske, and W. Fuhs, *Thin Solid Films* **330**, 108 (1998).
- ³⁶M. D. McCluskey and S. J. Jokela, *J. Appl. Phys.* **106**, 071101 (2009).
- ³⁷A. Janotti and C. G. V. de Walle, *Appl. Phys. Lett.* **87**, 122102 (2005).
- ³⁸K. Ellmer and R. Mientus, *Thin Solid Films* **516**, 4620 (2008).
- ³⁹S. Cornelius, M. Vinnichenko, N. Shevchenko, A. Rogozin, A. Kolitsch, and W. Möller, *Appl. Phys. Lett.* **94**, 042103 (2009).
- ⁴⁰K. Ellmer and R. Mientus, *Thin Solid Films* **516**, 5829 (2008).
- ⁴¹J. Y. W. Seto, *J. Appl. Phys.* **46**, 5247 (1975).
- ⁴²G. Baccarani, B. Riccò, and G. Spadini, *J. Appl. Phys.* **49**, 5565 (1978).
- ⁴³*Transparent Conductive Zinc Oxide: Basics and Applications in Thin Film Solar Cells*, edited by K. Ellmer, A. Klein, and B. Rech, Springer Series in Materials Science (Springer, Berlin, 2008).
- ⁴⁴N. F. Mott, *Metal-Insulator Transitions* (Taylor & Francis, London, 1990).
- ⁴⁵D. H. Zhang and H. L. Ma, *Appl. Phys. A Mater.* **62**, 487 (1996).
- ⁴⁶E. Burstein, *Phys. Rev.* **93**, 632 (1954).
- ⁴⁷T. S. Moss, *Proc. Phys. Soc. B* **67**, 775 (1954).
- ⁴⁸D. G. Thomas, *J. Phys. Chem. Solids* **15**, 86 (1960).
- ⁴⁹A. Schleife, C. Rödl, F. Fuchs, J. Furthmüller, F. Bechstedt, P. H. Jefferson, T. D. Veal, C. F. McConville, L. F. J. Piper, A. DeMasi, K. E. Smith, H. Lösch, R. Goldhahn, C. Cobet, J. Zúñiga-Pérez, and V. Muñoz-Sanjosé, *J. Korean Phys. Soc.* **53**, 2811 (2008).
- ⁵⁰A. Schleife, C. Rödl, F. Fuchs, J. Furthmüller, and F. Bechstedt, *Appl. Phys. Lett.* **91**, 241915 (2007).
- ⁵¹H. Peelaers, E. Kioupakis, and C. G. Van de Walle, *Appl. Phys. Lett.* **100**, 011914 (2012).
- ⁵²E. Kioupakis, P. Rinke, A. Schleife, F. Bechstedt, and C. G. Van de Walle, *Phys. Rev. B* **81**, 241201 (2010).
- ⁵³A. Schleife, C. Rödl, F. Fuchs, J. Furthmüller, and F. Bechstedt, *Phys. Rev. B* **80**, 035112 (2009).
- ⁵⁴A. Schleife, Ph.D. thesis, Friedrich-Schiller-Universität, Jena, 2010. Electronic and optical properties of MgO, ZnO, and CdO (Südwestdeutscher Verlag für Hochschulschriften, 2011).
- ⁵⁵K. F. Berggren and B. E. Sernelius, *Phys. Rev. B* **24**, 1971 (1981).
- ⁵⁶U. Özgür, Y. I. Alivov, C. Liu, A. Teke, M. A. Reshchikov, S. Doğan, V. Avrutin, S.-J. Cho, and H. Morkoç, *J. Appl. Phys.* **98**, 041301 (2005).